Article

Spectral response of aluminium oxide and copper-doped zinc sulphide antireflection nanostructures for photovoltaic applications

E. Bwayo[1,2,*], W. K. Njoroge[1], J. Okumu[1] and D. Mukiibi[3]

[1]   Department of Physics, School of Physical and Applied Sciences, Kenyatta University, P. O. Box 43844-00100, Nairobi-Kenya.

[2]   Department of Physics, Faculty of Science, Muni University, P. O. Box 725, Arua-Uganda.

[3]   Department of Physics, School of Physical Sciences, College of Natural Sciences, Makerere University, P. O. Box 7062, Kampala- Uganda.

*   Correspondence: bwayoedward@gmail.com

Abstract: The performance of an antireflection coating entirely depends on the proportion of light energy transmitted or reflected by the coating material. To enhance the transmittance of an antireflection coating, evaluation of the amount of the light energy transmitted to generate charge carriers is very critical. Thus, in this paper, we demonstrate the effect of sputtering power and gas flow rate on the optical transmittance of aluminium oxide (Al_2O_3) and copper-doped zinc sulphide (ZnS:Cu) antireflection nanostructures. To this end, radiofrequency sputtering was used for the deposition of ZnS:Cu, using the ZnS:Cu target ($94/6.0\%$) using argon (99.9% pure), and direct current sputtering was used for the deposition of Al_2O_3 using the aluminium target (99.99% purity) and oxygen (99.9% pure). The gas flow rates of 40 to 100 sccm were used. The sputtering power values of 70 W to 140 W were used at a low process pressure of 6.5×10^{-3}. The transmittance was observed to decrease with an increase in sputter power and deposition time. However, the transmittance of single-layer nanofilms was lower than that of the double-layer nanostructures. For photovoltaic applications, the Al_2O_3/ZnS:Cu(112.1 nm) nanostructure exhibited the highest transmittance of 96.9% at $\lambda = 780$ nm. The reflectance of the nanostructures increased with an increase in coating time and sputtering power, with the lowest value of 3.03% recorded at 360 nm. The nanostructures are crystalline, smooth, and dense but the crystallite sizes decreased from 0.02508 to 0.02071 Å with an increase in gas flow rate. This decrease in crystallinity was due to the reduced adatom migration on the substrate. The optimal gas flow rate was 100 sccm, in which the Al_2O_3/ZnS:Cu(117 nm) had the highest transmittance of 97.7% at $\lambda = 741$ nm. The results demonstrate the potential use of Al_2O_3/ZnS:Cu nanostructures as antireflection materials for photovoltaic solar cells.

Keywords: Kernels, Lagrangian multiplier, least square, Olanrewaju-Olanrewaju regression-type, nonparametric regression, support vector regressor (SVR).

1. Introduction

The performance of photovoltaic solar cells is hinged on the amount of solar energy absorbed by the active layer of the solar cell. The amount of light energy transmitted through the top cover of the solar cell determines how much of the light energy is absorbed by the solar cell [1,2]. The solar cell's top cover significantly influences the transmission of incident radiation into the solar cell. However, not all the light that is incident is transmitted and consequently absorbed, but a fraction is lost through reflection and scattering, which ultimately lowers the cell's efficiency [3].

Therefore, it is very vital to fabricate nanostructures that have high transmittance but low reflectance to short-wavelength ultraviolet, visible, and near-infrared radiations [4,5]. Although single layer antireflection coatings have been demonstrated, double- or multiple-layer dielectric thin films are being adopted to attenuate the intensity of light energy reflected by the solar cell [6,7].

In the recent past, [8] used magnetron sputtering to prepare ZnS thin films on glass. The transmittance was predominantly low, and it ranged between 63.0% and 95.7% in the visible spectrum. Furthermore, [9] used magnetron sputtering to coat ZnS thin films on bare polycrystalline silicon cell and obtained an average transmittance of 90%. The zinc sulphide was used because of its high refractive index (2.35) and wide band gap (3.7 eV), which reduce absorption losses in the short wavelength spectrum and thus improve short-circuit current.

Relatedly, [10] characterised Al_2O_3 thin films prepared by magnetron sputtering at different sputtering powers and argon pressures. Transmittance values of 92% to 94% were obtained, while the reflectance values ranged from 7% to 10%. The Al_2O_3 was selected because it is stable and does not easily degrade in the environment [11,12]. Secondly, Al_2O_3 has a high band gap of 5.1-8.8 eV for different crystallographic structures [13].

The transmission and reflection processes occurring in the double layers produce either constructive and/or destructive interference effects. Destructive interference is of great importance in the design of antireflection nanofilms. Destructive interference occurs when the incident light energy is reflected out of phase by 180° into the incident medium [14]. The phenomenon of destructive interference is influenced by several factors ranging from film thickness, microstructure, film density, and surface morphology. However, the energy changes that take place on the front cover of the solar cell [15] are governed by the relation:

$$T + R + A = 1, \tag{1}$$

where A, T, and R are the absorbance, transmittance, and reflectance [16]. The amount of reflection that occurs due to refractive index change at an interface at normal incidence [17,18] is defined by the equation:

$$R = \left(\frac{n_p - n_m}{n_p + n_m} \right)^2, \tag{2}$$

where n_p is the refractive indices of the thin film and and n_m is the refractive index air [17]. The amount of light energy transmitted T, through a material of thickness t, is calculated from the reflectance R and absorption coefficient α of the transmitting material as follows:

$$T = \frac{1}{t} \frac{\ln(1 - R)^2}{\alpha}. \tag{3}$$

Thus, in this work, we demonstrate the effect of deposition time, sputtering power, and argon and oxygen flow rate on the spectral transmittance of Al_2O_3 and ZnS:Cu antireflection nanostructures.

2. Materials and Methods

The indium tin oxide substrate was cleaned in an ultrasonic bath containing a solution of sodium stearate soap for 15 minutes and later rinsed with distilled water, ethanol, and acetone for ten minutes. The substrates were then dried in the air using argon gas. The substrates were then placed 14 cm vertically above the target in the vacuum chamber. The Edwards 306 magnetron sputtering machine was used for the preparation of thin films [19,20]. Radiofrequency sputtering was used for the deposition of copper-doped zinc sulphide ZnS:Cu (94/6.0% copper) onto the substrate using argon (99.9% pure) as a working gas. The argon gas flow rates used were 40, 70, and 100 sccm. The radio frequency sputtering power values of 70 W, 100 W, and 140 W were also used at a low process pressure of 6.5×10^{-3} for 5, 10, 20, and 30 minutes.

Direct current (D.C.) reactive sputtering was used for the deposition of aluminium oxide using the aluminium (Al) target (99.99% purity) and oxygen (99.9% pure). The chamber was pumped down to a high vacuum of 5.5×10^{-5} mBar before sputtering was allowed to take place. The process proceeded by allowing oxygen gas into the chamber at gas flow rates of 40, 70, and 100 sccm. The D.C. power values of 70 W, 100 W, and 140 W were used. The D.C. sputtering was allowed to take place at a low process pressure of 6.5×10^{-3} mBars for 5, 10, 20, and 30 minutes. The high-energy oxygen ions hit the Al target, causing target atoms to break off to form aluminium vapour [21]. The oxygen ions react with Al atoms to form Al_2O_3 [22,23] vapour, which is transported to the substrate.

The Al_2O_3 films were deposited onto the ZnS:Cu/ITO substrate to form the Al_2O_3/ZnS:Cu/ITO double-layer structure. In both methods, the target-to-substrate distance was set to 14 cm. The flow of argon and oxygen gases was controlled by the Alicat Scientific (MC-100SCCM-D/5M, 5IN) (Tucson, AZ, USA), and the samples were uniformly rotated by a rotary workholder connected to the rotary workholder drive. After the Al_2O_3/ZnS:Cu films had been deposited, the samples were removed from the vacuum chamber and kept in an incubator containing calcium oxide. The sample's thickness was then measured by the Alpha-Step IQ surface profiler by taking measurements at three different points across the length of the film. An average value of film thickness was computed and recorded.

The samples' transmittance and reflectance were measured by the spectrophotometer, model Solidspec-3700 DUV, in the wavelength range of 200 to 800 nm. The microstructure of the samples was studied by the x-ray diffractometer machine, ARL Equinox 100. The copper anode (Cu K_α radiation) was used with an x-ray emission wavelength of 1.54056 Å with a scan time of 240 s. The film roughness was studied by the scanning electron microscope (SEM) (model ZEISS) operating at 6.00 kV, WD of 9.6 mm, and signal A = SE2. The samples were analysed after sample treatment with chromium as the electron-conducting material.

3. Results and Discussion

3.1. Single layer nanostructures

3.1.1. Transmittance and reflectance

The transparent single-layer Al_2O_3 and ZnS:Cu nanostructures formed with different film thicknesses have been analysed as shown in Figure 1(a). The transmittance of the nanofilms increased from the short-wavelength ultraviolet band toward the long-wavelength visible spectrum. However, interference effects observed in the ZnS:Cu films were due to reflections from the film and substrate interfaces [24]. This is because highly crystallised nanostructures exhibit fewer defects [25], grain boundaries, and structural imperfections, which reduces the scattering of light energy. This effect enhances the transmittance of visible light [9,26].
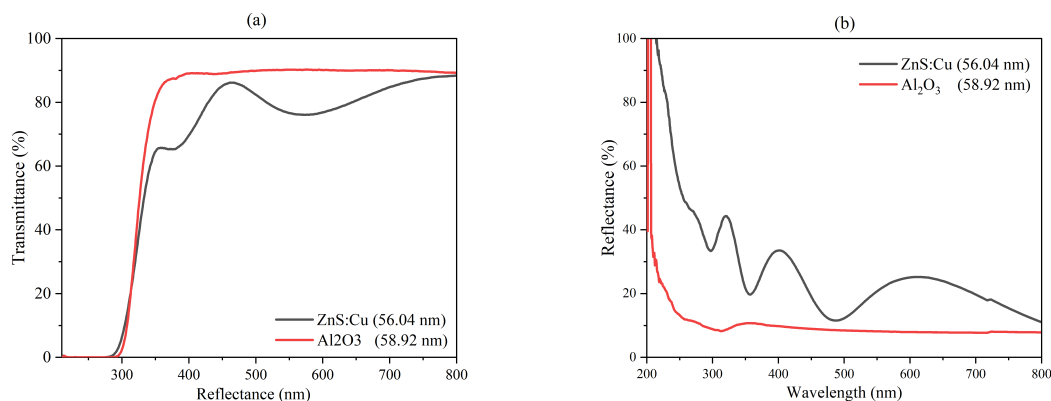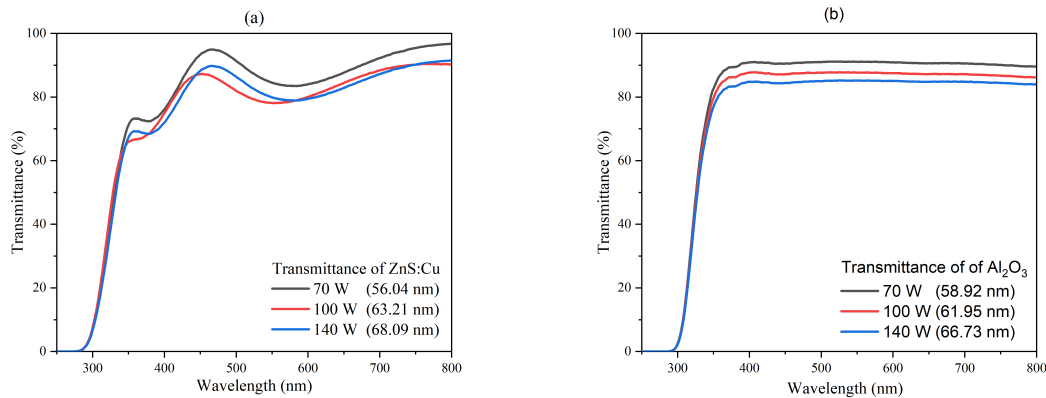

Figure 1. (a) Transmittance of single-layer antireflection nanostructures of ZnS:Cu (56.04 nm) and Al_2O_3 (58.94 nm) (b) Reflectance of single-layer antireflection nanostructures of ZnS:Cu (56.04 nm) and Al_2O_3 (58.94 nm) sputtered at 70 W with argon and oxygen flow rate of 40 sccm

To visualise how much of the incident energy was reflected, the reflectance characteristics of Al_2O_3 and ZnS:Cu are presented in Figure 1(b). The reflectance of ZnS:Cu(56.04 nm) was recorded to be 11.94% at the wavelength $\lambda = 488$ nm. Interference effects were observed in the reflectance spectra of ZnS:Cu(56.04 nm). The reflectance of Al_2O_3(58.92 nm) thin films was 7.19%. The recorded reflectance values are relatively high. Moreover, [27] argued that the shortcomings of a single-layer antireflection coating include the reduction in reflectance over limited wavelengths [28].

3.1.2. Sputtering power and film thickness

The transmittance of single-layer ZnS:Cu nanostructures (Figure 2(a)) was observed to decrease with an increase in sputtering power. An absorption edge in the ultraviolet region with a red shift in the fundamental absorption edge, which increased with sputtering power and film thickness. Furthermore, at the absorption edge, the transmittance for different sputtering powers is 73.49%, 66.86%, and 69.43% for 70 W, 100 W, and 140 W, respectively. The transmittance of Al_2O_3 nanostructures (Figure 2(b)) was observed to increase from the short wavelength towards the long wavelength part of the electromagnetic spectrum. The highest

Figure 2. (a) Variation of transmittance with sputtering power (film thickness) (a) Single-layer ZnS:Cu, (b) single-layer Al_2O_3 nanostructures

transmittance of 91.45%, 88.14%, and 85.20% was obtained for the films sputtered at 70 W, 100 W, and 140 W, respectively. A related study by [10] on the optical properties of Al_2O_3 gave maximum transmittance of 92% and reflectance of approximately 7.8%. However, low deposition power results in a slow deposition rate, leading to small film thickness with lower density, which increases the scattering of light energy. At higher sputtering power, the films form a dense and uniform microstructure, which decreases transmittance [29,30]. Therefore, based on the transmittance data discussed in this section, the single-layer nanostructures will require modification to lower the transmittance of light energy in the entire electromagnetic spectrum.

3.2. Double-layer nanostructures

3.2.1. Effect of deposition time and film thickness

The transmittance spectra for the transparent Al_2O_3/ZnS:Cu thin nanofilms are shown in Figures 3. An increase in the deposition time increased the transmittance because the substrate receives more ionised atoms for deposition, hence an increase in film thickness [31]. The transmittance of the ITO blank was generally lower than for the coated films. This shows an improvement in the transmission characteristic of the Al_2O_3/ZnS:Cu nanostructures [32]. The highest the transmittance values ranged between 72 and 98%, which highlight good antireflection properties. The high transmission was due to reduced scattering and micro defects in the nanostructures [33,34] and high film homogeneity.

A comparative study of the reflectance of Al_2O_3/ZnS:Cu thin nanofilms deposited at a sputtering power of 70 W is presented in Figure 3(b). The reflectance of Al_2O_3/ZnS:Cu nanostructure increased with an increase in deposition time. This reciprocal behaviour in transmittance and reflectance satisfies the energy balance condition of equation (1.1), assuming there is no absorption in the thin films [14,16]. The effective reflectance of the nanostructures decreased significantly and approached minimum values of 3.03% to 4.61% in the ultraviolet region and 9.08% to 11.38% in the visible region. The shape of the reflectance curve, according to [35], corresponds to the requirement for a well-matched refractive index gradient. This spectral behaviour was also observed by [27] and [35].
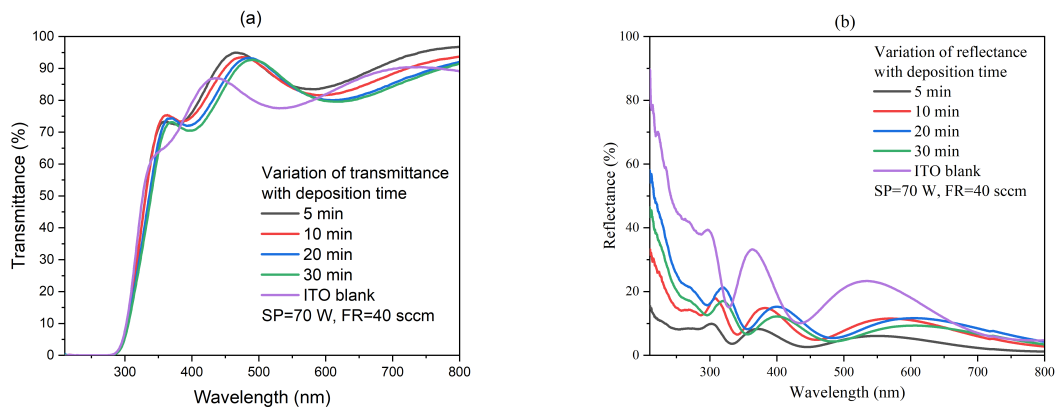
Figure 3. Effect of deposition time on (a) Transmittance of Al_2O_3/ZnS:Cu (b) Reflectance of Al_2O_3/ZnS:Cu sputtered at 70 W and argon flow rate of 40 sccm

3.2.2. Variation of sputtering power and gas flow rate on transmittance

The variation of transmittance with sputtering is presented in Figure 4(a). The transmittance gradually decreased as the power was raised from 70 W to 140 W. At low sputtering power, in the presence of the sputtering gas, the sputtered ions were thermalised by collision during the transition to the substrate. Therefore, less energetic ions can hardly diffuse across the surface of the substrate, resulting in poor crystallinity in the growing film [36]. When the sputtering power was raised, the sample's film thickness increased due to the high rate of deposition [37], which increased the grain size of the nanofilms. This makes the surface rough and results in the enhanced scattering of light energy. This is the reason for the observed decrease in the transmittance as the sputtering power increases [38].
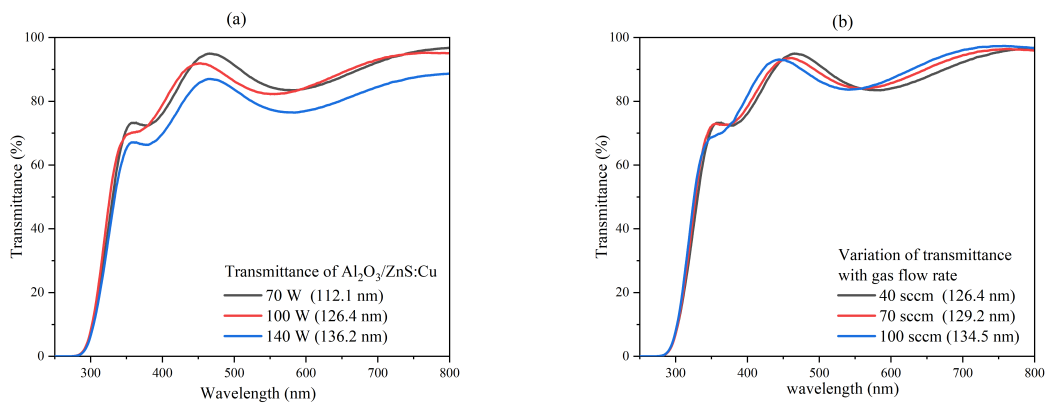
Figure 4. (a) Effect of sputtering power on Al_2O_3/ZnS:Cu nanostructures sputtered with argon and oxygen flow rate of 40 sccm for 5 minutes (b) Effect of gas flow rate on transmittance of Al_2O_3/ZnS:Cu nanostructures sputtered at 70 W

In Figure 4(b), the transmittance curves for different flow rates increased from the short wavelength to the long wavelength with overlaps in intensity at different wavelengths. Nonetheless, the effect of gas flow rate did not have a clear-cut effect on the transmittance of the nanostructures due to overlaps along the spectrum. However, an increase in gas flow rate causes high collision rates between the gas molecules and sputtered ions. This can result in rougher or more porous films, which can scatter light, thus decreasing the optical transmittance. Additionally, high flow rates may introduce more impurities or contaminants into the film, further reducing transmittance [39,40].
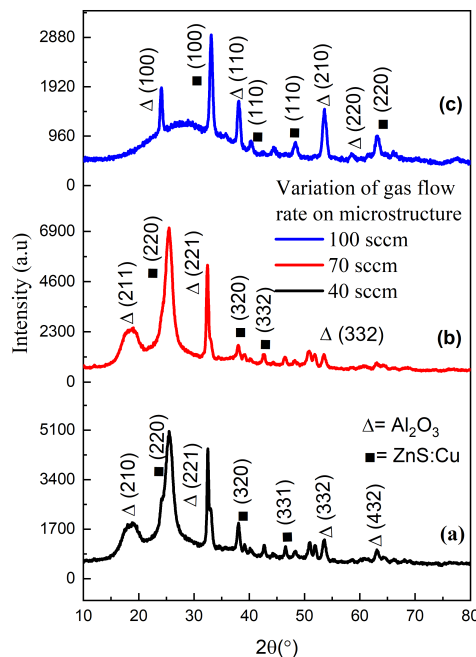
3.2.3. Microstructure

The microstructure of $Al_2O_3/ZnS{:}Cu$ nanofilms formed at different argon and oxygen flow rates is shown in Figure 5. The crystallite size of the samples was calculated by the modified Scherrer formula [41] according to:

$$\ln \beta = \ln \left(\frac{K\lambda}{D_{hkl}} \right) + \ln \left(\frac{1}{\cos \theta} \right). \qquad (4)$$

The acceptable intercept is obtained when the *slope* ≈ 1.

When a graph of $\ln \beta$ was plotted against $\ln(\frac{1}{\cos \theta})$ a straight line was obtained with an intercept c equal to $\ln \frac{K\lambda}{D_{hkl}}$ along the $\ln \beta$ axis [42]. The shape factor, $k \approx 0.9$, D_{hkl} is the crystallite size, λ is the wavelength of x-rays, θ is the diffraction angle, and β is the full width at half maximum (FWHM) of the diffraction peak [43]. It was noted that all the multilayers are crystalline with strong peak intensities located between $2\theta = 25.43^o$ and 36.44^o. A strong peak for the (220) crystallographic plane belongs to ZnS according to ICSD card number 67453.

This peak appears in nanofilms formed during the gas flow rates of 40 sccm and 70 sccm. This plane reveals cubic ZnS structure, which was also reported by [33] according to card number: PDF 05-0566. Another dominant peak of (221) was assigned to Al_2O_3 crystallographic planes according to ICSD CODE 9770. These planes were preferred because their formation energy was lower than the surface energy of other lattice planes [44,45]. However, Cu-related diffraction peaks from ZnS:Cu were not observed in the XRD patterns. This is because the copper (II) ions only act as foreign particles in the ZnS lattice, in which the cooper (II) occupy Zn sites in the ZnS lattice. This similar behaviour was reported by [33].

Figure 5. Effect of gas flow rate on microstructure of $Al_2O_3/ZnS{:}Cu$ double layer films formed by depositing for 5 minute with sputtering power of 100 W for: (a) Gas flow rate of 40 sccm, (b) Gas flow rate of of 70 sccm, (c) Gas flow rate of 100 sccm

The changes in peak intensities had a proportionate decrease in the crystallite size from 0.02508 to 0.02071 Å, Table 1. Separate studies by [46] and [47] revealed that the decrease in crystallinity and hence grain size of the crystallites was attributed to the increase in the argon and oxygen gas flow rates. Further explanation by [39] asserts that an increase in argon flow rate increases the background pressure of the gas, which consequently decreases the rate of film growth.

This observation was earlier explained by [48] that at long target substrate distances, the high-velocity argon atoms tend to take away low-energy sputtered atoms. This implies that some of the low-energy atoms

are less likely to reach the substrate, thus making the growth rate drop as the flow rate increases [49]. The crystallite sizes of the samples were analysed by the modified Scherrer formula:

$$\ln \beta = \ln \left(\frac{K\lambda}{D_{hkl}} \right) + \ln \left(\frac{1}{\cos \theta} \right).$$

(5)

Plotting a graph of $\ln \beta$ against $\ln(\frac{1}{\cos \theta})$ gives a straight line with an intercept c equal to $\ln \frac{K\lambda}{D_{hkl}}$ along the $\ln \beta$ axis [42]. The shape factor, $k \approx 0.9$, D_{hkl} is the crystallite size, λ is the wavelength of x-rays, θ is the diffraction angle of a particular diffraction peak, and β is the full width at half maximum (FWHM) of the diffraction peak corresponding to a given crystal plane [43].

Table 1. Variation of gas flow rate (GFR) with crystallite size (D_{hkl}) and FWHM and dislocation density δ of $Al_2O_3/ZnS:Cu$ thin films

GFR (sccm)	2θ	d (Å)	FWHM (^{o})	D_{hkl} (nm)	δ (nm^{-2})
40	27.18	2.795	3.116	0.02508	1589.8
70	25.47	2.675	3.370	0.02278	1927.0
100	25.47	2.621	3.831	0.02071	2331.5

When the increase in gas flow rate was raised, the FWHM also increased which indicates that the crystallinity of the films was deteriorating, and hence, the crystallite size of the $Al_2O_3/ZnS:Cu$ nanoparticles decreased with an increase in the gas flow rate. According to [50] and [51], the decrease in crystallite size was due to defects or dislocations generated during film formation. This trend was also reported by [52]. The lattice parameter d for crystallite structure for different flow rates was calculated from the Bragg's law equation [40,53].

3.2.4. Surface morphology

The morphological images of transparent $Al_2O_3/ZnS:Cu$ nanostructures sputtered with argon and oxygen flow rates of 40, 70, and 100 sccm are shown in Figure 6. The $Al_2O_3/ZnS:Cu$ nanofilms were found to be continuous and dense. At a low gas flow rate of 40 sccm (Figure 6(a)), the Al_2O_3 and ZnS:Cu particles are uniformly distributed over the surface of the substrate. There is a decrease in crystallinity due to the reduced number of atoms migrating on the surface of the substrate. This is because an increase in gas flow rate reduces the mean free path of the sputtered ions and hence increases the number of ions in the plasma [39]. This increases the probability of interionic collisions that result in the reduction of the number of ions per second reaching the substrate. Nonetheless, further increase in gas flow rate to 100 sccm led to the non-uniform distribution of sputtered particles on the substrate's surface. This is because during the deposition, agglomerations of both Al_2O_3 and ZnS:Cu are formed as a result of the low rate of nucleation on the surface of the substrate [9].
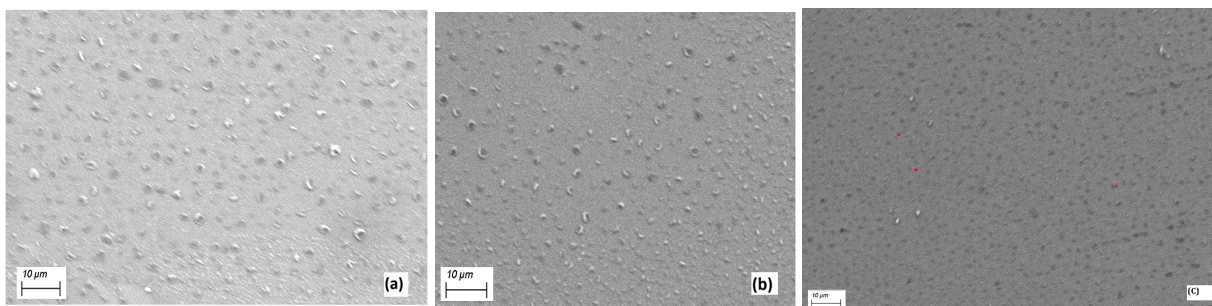
Figure 6. Effect of argon and oxygen flow rate on surface morphology of $Al_2O_3/ZnS:Cu$ nanostructures sputtered for 20 minutes at 100 W. (a) 40 sccm, (b) 70 sccm (c) 100 sccm

4. Conclusions

The transmittance spectra data for the Al_2O_3 and ZnS:Cu nanostructures show single-layer nanostructures had lower transmittance values than double-layer nanostructures. Double-layer nanostructures had above-average transmittance values (68.11% to 75.44%) in the ultraviolet region and the highest transmittance (78.85% and 96.63%) in the visible region. However, the transmittance was observed to decrease with an increase in sputtering power and deposition time. The low values of reflectance are highly commendable for photovoltaic antireflection nanostructures. The effective reflectance of the nanostructures decreased significantly and approached minimum values of 3.03% to 4.61% in the ultraviolet region and 9.08% to 11.38% in the visible spectrum. The nanostructures are crystalline with strong peak intensities located at $2\theta = 25 - 43^o$. Nonetheless, the crystallite sizes decreased from 0.02508 to 0.02071 Å as the gas flow rate increased from 40 to 100 sccm. This decrease in crystallinity was due to the reduced number of atoms migrating on the surface of the substrate. The morphology of the deposited ZnS:Cu films was found to be smooth, continuous, and dense. The results demonstrate that the double-layer Al_2O_3 and ZnS:Cu nanostructures are highly commendable for use as antireflection materials for the top cover photovoltaic solar cells.

Author Contributions: E. Bwayo, W. Njoroge, J. Okumu: sample preparation, and spectroscopic analysis; E. Bwayo and D. Mukiibi: analysis of microstructure and surface morphology. All authors participated in manuscript write up.

Conflicts of Interest: We the authors certify that there is no conflict of interest whatsoever with any affiliation, or involvement with any organization, financial and non-financial entity.

References

[1] Doroody, C., Rahman, K. S., Kiong, T. S., & Amin, N. (2022). Optoelectrical impact of alternative window layer composition in CdTe thin film solar cells performance. *Solar Energy, 233*, 523–530.

[2] Reuna, J., Hietalahti, A., Aho, A., Isoaho, R., Aho, T., Vuorinen, M., Tukiainen, A., Anttola, E., & Guina, M. (2022). Optical performance assessment of nanostructured alumina multilayer antireflective coatings used in III–V multijunction solar cells. *ACS Applied Energy Materials, 5*(5), 5804–5810.

[3] Soonmin, H. (2020). Analysis of thin films by infrared spectroscopy. *Ind. J. Nat. Sci., 10*, 27593–27599.

[4] Keshavarz Hedayati, M., & Elbahri, M. (2016). Antireflective coatings: Conventional stacking layers and ultrathin plasmonic metasurfaces, a mini-review. *Materials, 9*(6), 497.

[5] Tam, W., Yuen, W., & Chow, W. (2016). Numerical study on the importance of radiative heat transfer in building energy simulation. *Numerical Heat Transfer, Part A: Applications, 69*(7), 694–709.

[6] Cheng, C.-H., & Ting, J.-M. (2007). Transparent conducting GZO, Pt/GZO, and GZO/Pt/GZO thin films. *Thin Solid Films, 516*(2–4), 203–207.

[7] Yenisoy, A., Yesilyaprak, C., Ruzgar, K., & Tuzemen, S. (2019). Ultra-broad band antireflection coating at mid wave infrared for high efficient germanium optics. *Optical Materials Express, 9*(7), 3123–3131.

[8] Kong, L., Deng, J., & Chen, L. (2017). Structural and optical characterization of magnetron sputtered ZnS thin films annealed in different atmosphere. *Chalcogenide Letters, 14*(3).

[9] Gobinath, V., Rajasekar, R., Moganapriya, C., Sri, A. M., Raja, G., Kumar, P. S., & Jaganathan, S. (2021). Surface engineering of zinc sulphide film for augmenting the performance of polycrystalline silicon solar cells. *Chalcogenide Letters, 18*(7).

[10] García-Valenzuela, J. A., Rivera, R., Morales-Vilches, A. B., Gerling, L. G., Caballero, A., Asensi, J. M., ... & Andreu, J. (2016). Main properties of Al2O3 thin films deposited by magnetron sputtering of an Al2O3 ceramic target at different radio-frequency power and argon pressure and their passivation effect on p-type c-Si wafers. *Thin Solid Films, 619*, 288-296.

[11] Butanovs, E., Kuzmin, A., Zolotarjovs, A., Vlassov, S., & Polyakov, B. (2022). The role of Al_2O_3 interlayer in the synthesis of $ZnS/Al_2O_3/MoS_2$ core-shell nanowires. *Journal of Alloys and Compounds, 918*, 165648.

[12] Patnaik, P. (2003). *Handbook of inorganic chemicals* (Vol. 529). McGraw-Hill.

[13] Pustovarov, V., Perevalov, T., Gritsenko, V., Smirnova, T., & Yelisseyev, A. (2011). Oxygen vacancy in Al_2O_3: Photoluminescence study and first-principle simulation. *Thin Solid Films, 519*(19), 6319–6322.

[14] Lilhare, D., & Khare, A. (2020). Development of chalcogenide solar cells: Importance of CdS window layer. *Opto-Electronics Review, 28*.

[15] Sardela, M. (Ed.). (2014). *Practical materials characterization*. Springer.

[16] Ali, A. M. A. M. (2021). The optical properties of multilayers thin films. *Journal of Science and Technology NJST, 5*, 3033.

[17] Huang, L., Wang, T., Li, X., Wang, X., Zhang, W., Yang, Y., & Tang, Y. (2020). UV-to-IR highly transparent ultrathin diamond nanofilms with intriguing performances: Anti-fogging, self-cleaning and self-lubricating. *Applied Surface Science, 527*, 146733.

[18] Kennedy, S. R., & Brett, M. J. (2003). Porous broadband antireflection coating by glancing angle deposition. *Applied Optics, 42*(22), 4573–4579.

[19] Choudapur, V., Kapatkar, S., & Raju, A. (2019). Synthesis and characterization of Cu doped ZnS thin films deposited by spin coating.

[20] Fathima, M. I., & Wilson, K. J. (2019). Antireflection coating application of zinc sulfide thin films by nebulizer spray pyrolysis technique. In *AIP Conference Proceedings* (Vol. 2115, p. 030327). AIP Publishing LLC.

[21] Ejaz, H., Hussain, S., Zahra, M., Saharan, Q. M., & Ashiq, S. (2022). Several sputtering parameters affecting thin film deposition. *Journal of Applied Chemical Science International, 13*(3), 41–49.

[22] Baranowska-Korczyc, A., Kościński, M., Coy, E. L., Grześkowiak, B. F., Jasiurkowska-Delaporte, M., Peplińska, B., & Jurga, S. (2018). ZnS coating for enhanced environmental stability and improved properties of ZnO thin films. *RSC Advances, 8*(43), 24411–24421.

[23] Zarzycki, A., Dyndał, K., Sitarz, M., Xu, J., Gao, F., Marszałek, K., & Rydosz, A. (2020). Influence of GLAD sputtering configuration on the crystal structure, morphology, and gas-sensing properties of the WO_3 films. *Coatings, 10*(11), 1030.

[24] Soudi, J., Sandeep, K., Sarojini, B., Patil, P. S., Maidur, S. R., & Balakrishna, K. (2021). Thermo-optic effects mediated self-focusing mechanism and optical power limiting studies of ZnO thin films deposited on ITO coated PET substrates by RF magnetron sputtering under continuous wave laser regime. *Optik, 225*, 165835.

[25] Tariq, G. H., Asghar, G., Shifa, M. S., Anis-Ur-Rehman, M., Ullah, S., Shah, Z. A., Ziani, I., Tawfeek, A. M., & Sher, F. (2023). Effect of copper doping on plasmonic nanofilms for high performance photovoltaic energy applications. *Physical Chemistry Chemical Physics, 25*(46), 31726–31740.

[26] Grayeli, A., Ahmadpourian, A., Jurečka, S., Luna, C., Rezaee, S., & Karimi, M. (2024). Investigating the influence of RF power on the surface morphological and optical properties of sputtered TiO_2 thin films. *Optical Materials*, 116363.

[27] Shanmugam, N., Pugazhendhi, R., Madurai Elavarasan, R., Kasiviswanathan, P., & Das, N. (2020). Anti-reflective coating materials: A holistic review from PV perspective. *Energies, 13*(10), 2631.

[28] Kushnir, O. (2015). Simple expressions for the designing of the double bandpass optical filter. *ECONTECHMOD: An International Quarterly Journal on Economics of Technology and Modelling Processes, 4*.

[29] Gould, R. D., Kasap, S., & Ray, A. K. (2017). Thin films. In *Springer handbook of electronic and photonic materials* (pp. 1–1). Springer.

[30] Li, J., Ren, G.-K., Chen, J., Chen, X., Wu, W., Liu, Y., Chen, X., Song, J., Lin, Y.-H., & Shi, Y. (2022). Facilitating complex thin film deposition by using magnetron sputtering: A review. *JOM, 74*(8), 3069–3081.

[31] Lemarquis, F., Begou, T., Moreau, A., & Lumeau, J. (2019). Broadband antireflection coatings for visible and infrared ranges. *CEAS Space Journal, 11*, 567–578.

[32] Sharma, R., Amit, G., & Ajit, V. (2017). Effect of single and double layer antireflection coating to enhance photovoltaic efficiency of silicon solar.

[33] Ke, J., Chen, S., Song, L., Zhang, P., Cao, X., Wang, B., & Zhang, R. (2020). Effect of film thickness on structural and optical properties of ZnS:Cu films prepared by vulcanization. *Superlattices and Microstructures, 146*, 106671.

[34] Rehman Khan, A. U., Ramzan, M., Faisal Iqbal, M., Hafeez, M., Fadhali, M. M., Somaily, H. H., Javid, M., Waqas Mukhtar, M., & Farooq Saleem, M. (2024). Effect of the source to substrate distance on structural, optoelectronic, and thermoelectric properties of zinc sulfide thin films. *arXiv e-prints*, arXiv:2404.

[35] Yang, T., Wang, X., Liu, W., Shi, Y., & Yang, F. (2013). Double-layer anti-reflection coating containing a nanoporous anodic aluminum oxide layer for GaAs solar cells. *Optics Express, 21*(15), 18207–18215.

[36] Rossnagel, S., Yang, I., & Cuomo, J. (1991). Compositional changes during magnetron sputtering of alloys. *Thin Solid Films, 199*(1), 59–69.

[37] Zhang, Z., Li, J., Zhou, Y., Fu, H., Zhang, Z., Xiang, G., Zhao, Y., Zhuang, S., Yang, F., & Wang, H. (2019). Effect of sputtering power on the structural and optical properties of InN nanodots on Al_2O_3 by magnetron sputtering. *Materials Research, 22*(6), e20190380.

[38] Priyadarshini, B. G., & Sharma, A. K. (2016). Design of multi-layer anti-reflection coating for terrestrial solar panel glass. *Bulletin of Materials Science, 39*, 683–689.

[39] Atta, A., Hassanien, A., El-Nahass, M., Shaltout, A. A., Al-Talhi, Y. A., & Aljoudi, A. M. (2019). Influence of argon flow rate on structural and optical properties of transparent Nb_2O_5 thin films. *Optical and Quantum Electronics, 51*, 1–17.

[40] Bashar, M., Matin, R., Sultana, M., Siddika, A., Rahaman, M., Gafur, M., & Ahmed, F. (2020). Effect of rapid thermal annealing on structural and optical properties of ZnS thin films fabricated by RF magnetron sputtering technique. *Journal of Theoretical and Applied Physics, 14*, 53–63.

[41] Monshi, A., Foroughi, M. R., & Monshi, M. R. (2012). Modified Scherrer equation to estimate more accurately nano-crystallite size using XRD. *World Journal of Nano Science and Engineering, 2*(3), 154–160.

[42] Nasiri, S., Rabiei, M., Palevicius, A., Janusas, G., Vilkauskas, A., Nutalapati, V., & Monshi, A. (2023). Modified Scherrer equation to calculate crystal size by XRD with high accuracy, examples Fe_2O_3, TiO_2 and V_2O_5. *Nano Trends, 3*, 100015.

[43] Abed, A. M., Elttayef, A. K., & Razeg, K. H. (2019). Effect of thickness on structural and optical properties of ZnS: Mn films prepared by RF magnetron sputtering method. *Tikrit Journal of Pure Science, 24*(5), 65–69.

[44] Pelleg, J., Zevin, L., Lungo, S., & Croitoru, N. (1991). Reactive-sputter-deposited TiN films on glass substrates. *Thin Solid Films, 197*(1–2), 117–128.

[45] Zhao, J., Wang, X., Chen, Z. Y., Yang, S., Shi, T., & Liu, X. (1997). Overall energy model for preferred growth of TiN films during filtered arc deposition. *Journal of Physics D: Applied Physics, 30*(1), 5.s

[46] Khojier, K., Savaloni, H., Shokrai, E., Dehghani, Z., & Dehnavi, N. Z. (2013). Influence of argon gas flow on mechanical and electrical properties of sputtered titanium nitride thin films. *Journal of Theoretical and Applied Physics, 7*, 1–6.

[47] Yu, G., Tay, B., Lau, S. P., Prasad, K., Pan, L., Chai, J., & Lai, D. (2003). Effects of N ion energy on titanium nitride films deposited by ion assisted filtered cathodic vacuum arc. *Chemical Physics Letters, 374*(3–4), 264–270.

[48] Lu, L., Shen, H., Zhang, H., Jiang, F., Li, B., & Lin, L. (2010). Effects of Ar flow rate and substrate temperature on the properties of AZO thin films by RF magnetron sputtering. *Growth, 8*, 9.

[49] Arshi, N., Lu, J., Joo, Y. K., Lee, C. G., Yoon, J. H., & Ahmed, F. (2012). Study on structural, morphological and electrical properties of sputtered titanium nitride films under different argon gas flow. *Materials Chemistry and Physics, 134*(2–3), 839–844.

[50] Hwang, D. H., Ahn, J. H., Hui, K. N., Hui, K. S., & Son, Y. G. (2012). Structural and optical properties of ZnS thin films deposited by RF magnetron sputtering. *Nanoscale Research Letters, 7*, 1–7.

[51] Valenzuela, A. A., & Russer, P. (1989). High Q coplanar transmission line resonator of $YBa_2Cu_3O_{7-x}$ on MgO. *Applied Physics Letters, 55*(10), 1029–1031.

[52] Simbrunner, J., Salzmann, I., & Resel, R. (2023). Indexing of grazing-incidence X-ray diffraction patterns. *Crystallography Reviews, 29*(1), 19–37.

[53] Akhtaruzzaman, M., Shahiduzzaman, M., Amin, N., Muhammad, G., Islam, M. A., Rafiq, K. S. B., & Sopian, K. (2021). Impact of Ar flow rates on micro-structural properties of WS_2 thin film by RF magnetron sputtering. *Nanomaterials, 11*(7), 1635.